8-1-2021

Efficient model for electronic transport in high energy-density matter

Liam G. Stanton
San Jose State University, liam.stanton@sjsu.edu

Michael S. Murillo
Michigan State University

Recommended Citation

Liam G. Stanton and Michael S. Murillo. "Efficient model for electronic transport in high energy-density matter" *Physics of Plasmas* (2021). https://doi.org/10.1063/5.0048162

RESEARCH ARTICLE | AUGUST 02 2021

Efficient model for electronic transport in high energy-density matter

Liam G. Stanton ✉ ; Michael S. Murillo

Physics of Plasmas 28, 082301 (2021)
https://doi.org/10.1063/5.0048162

Physics of Plasmas ARTICLE scitation.org/journal/php

Efficient model for electronic transport in high energy-density matter

Cite as: Phys. Plasmas **28**, 082301 (2021); doi: 10.1063/5.0048162
Submitted: 24 February 2021 · Accepted: 6 July 2021 ·
Published Online: 2 August 2021

Liam G. Stanton[1,a)] and Michael S. Murillo[2,b)]

AFFILIATIONS

[1]Department of Mathematics and Statistics, San José State University, San José, California 95192, USA
[2]Department of Computational Mathematics, Science and Engineering, Michigan State University, East Lansing, Michigan 48824, USA

Note: This paper is part of the Special Collection: Transport in Non-Ideal, Multi-Species Plasmas.
[a)]**Author to whom correspondence should be addressed:** liam.stanton@sjsu.edu
[b)]murillom@msu.edu

ABSTRACT

A wide-ranging effective Boltzmann approach, originally intended for ionic transport, is applied to the computation of electronic transport coefficients without modification. Comparisons with datasets that resulted from a recent transport coefficient workshop and molecular dynamics simulations are made. While this model contains correlation information through its effective potential and strong scattering through its use of cross sections, it misses details of attractive, possibly quantum, interactions; comparisons with that dataset reveal the relative importance of these physics inputs. Through comparisons of data for electrical conductivity, thermal conductivity, temperature relaxation, and stopping power (including a new formula for the energy split due to alpha stopping), we find that the sensitivity to the missing physics is minor and often negligible. Thus, we have a single transport model that self-consistently provides all ionic and electronic transport properties in a form with negligible computational cost.

I. INTRODUCTION

Plasma dynamics are determined in large part by energy transport, which includes thermal conductivity, electrical conductivity, temperature relaxation, and stopping power. Accurate and efficient models for the transport coefficients associated with these transport processes are necessary inputs to large-scale hydrodynamic simulations of plasmas; however, this can be quite challenging as energy transport in plasmas is typically dominated by electronic interactions, thus requiring more complicated models. The interpretation of many high energy-density experiments relies on self-consistent knowledge of multiple plasma properties.[1]

In this work, we apply the ionic Stanton and Murillo transport (SMT) model[2] to electronic transport phenomena, which was not its intended purpose; however, the efficiency of the model makes exploring its accuracy for these applications of interest. The SMT model is based on numerically calculated cross sections that are informed with effective binary interactions within a Boltzmann equation framework.[3–7] In this model, the underlying inter-particle interactions are assumed to be well-described by a screened Coulomb potential of the form

$$u_{ij}(r) = \frac{Z_i Z_j e^2}{r} e^{-r/\lambda_{\rm eff}}, \tag{1}$$

where r is the distance between particles, and Z_{ie} and Z_{je} are the *effective* charges of each charged species (CGS units have been used here and will be used for the remainder of the paper). These effective charges are formally the mean ionization states of each species that are determined from an average atom calculation to separate the bound (localized) and free (continuum) electronic states.[8] In doing so, the bound electrons and nuclei can be well-approximated as point charges with these mean ionization values, while the remaining free electrons contribute to the screening. A Thomas-Fermi model and its multi-component generalization are used to determine the mean ionization state in the current paper;[2,9,10] however, it would be interesting to better understand how sensitive the overall results are to the choice in ionization model.

In the SMT model, the effective binary potential is constrained to have the Yukawa form (1) to allow for rapid computation and simple fitting. The many-body physics is included through the effective screening length $\lambda_{\rm eff}$ that includes the total mean-field contribution as well as correlation information important for strongly coupled

plasmas. The choice of λ_{eff} in the SMT model has been shown to agree well with existing simulation data[2] and is given by

$$\lambda_{\text{eff}} = \left[\frac{1}{\lambda_e^2} + \sum_{i=1}^{N} \frac{1}{\lambda_i^2}\left(\frac{1}{1+3\Gamma_i^{\text{IS}}}\right)\right]^{-1/2}. \tag{2}$$

Here, the screening length of each ionic species is given by the relation $\lambda_i^{-2} = 4\pi Z_i^2 e^2 n_i/T$, where n_i is the number density of that species, and T is the temperature in units of energy. Formulas for the electron screening length can be found in Ref. 2, but a simple approximation with minimal error is given by

$$\lambda_e^{-2} \approx \frac{4\pi e^2 n_e}{\left(T^{9/5} + \left(\frac{2}{3}E_F\right)^{9/5}\right)^{5/9}}, \tag{3}$$

where n_e is the electronic number density, and $E_F = \hbar^2(3\pi^2 n_e)^{2/3}/2m_e$ is the Fermi energy. Finally, we have introduced the ion-sphere coupling parameter,

$$\Gamma_i^{\text{IS}} = \frac{(Z_i e)^2}{a_i T}, \tag{4}$$

which is expressed in terms of an ion-sphere radius that has been modified for mixtures as

$$a_i = \left(\frac{3Z_i e}{4\pi\rho_{\text{ion}}}\right)^{1/3}, \quad \rho_{\text{ion}} = \sum_{j=1}^{N} Z_j e n_j. \tag{5}$$

The term Γ_i^{IS} is included into the total screening length as a phenomenological way of accounting for strongly coupled ions. Once the effective screening length (2) is known, the plasma parameter $g_{ij} = Z_i Z_j e^2/(\lambda_{\text{eff}} T)$ can be calculated, where the relevant collision integrals $K_{nm}(g_{ij})$ associated with each transport process have been fitted to this parameter and can be found in Appendix C-3 of Ref. 2.

The SMT model has already been shown to be successful in comparison to both experiments and higher fidelity models; however, at first glance, it would seem inappropriate for Electron–electron and electron–ion interactions for two reasons:

(i) the interactions are assumed to be repulsive;
(ii) quantum diffraction effects are neglected.

However, we will show that disregarding both of these potential concerns is reasonable across a large swath of the parameter space for dense plasmas, thus creating a transport model that self-consistently provides all ionic and electronic transport properties in a form with negligible computational cost. The first of these issues is the simplest to understand as most transport coefficients scale to leading order as the charge of each species squared, and thus they do not depend on the sign of the charge of a given species. The breakdown of this scaling is the Barkas effect.[11,12] The latter issue is more complicated, but resonances associated with diffraction effects are often integrated out within the calculation of a given collision integral.[13]

The remainder of the manuscript is organized as follows. The SMT model is applied to both thermal and electrical conductivity in Sec. II, temperature relaxation in Sec. III, and stopping power in Sec. IV. Finally, concluding remarks are presented in Sec. V.

II. CONDUCTION

In this section, we discuss electrical and thermal conduction. We begin by reviewing different definitions of these quantities and the impact of their use in applications. We write the electronic (only) current density and energy flux in terms of Onsager coefficients $\{L_{ij}\}$ as[14]

$$-\mathbf{j}_p = L_{11}\frac{1}{T}\nabla\tilde{\mu} + L_{12}\nabla\left(\frac{1}{T}\right), \tag{6}$$

$$\mathbf{j}_E = L_{21}\frac{1}{T}\nabla\tilde{\mu} + L_{22}\nabla\left(\frac{1}{T}\right), \tag{7}$$

which contains thermal gradients ∇T as well as electrochemical forces $\nabla\tilde{\mu} = \nabla\mu - e\mathbf{E}$, where μ is the chemical potential, and $\mathbf{E}$ is the electric field. These terms would naturally arise in, for example, a Chapman-Enskog expansion,[5] and terms associated with other generalized forces may also appear (e.g., due to magnetic fields[14]). If these equations are used directly in a hydrodynamics model with known coefficients $\{L_{ij}\}$, the thermal conductivity coefficient is simply

$$\kappa_{\text{short}} = \frac{L_{22}}{T^2}. \tag{8}$$

This choice is referred to as the "short circuit" thermal conductivity because the current $\mathbf{j}_p$ is arbitrary: there is no assumed constraint among the gradients. Constraints can be imposed, such as isothermal, isobaric, adiabatic, or isochoric conditions, and the corresponding conductivities can be obtained accordingly.[15,16]

A common choice is the "open circuit" constraint that enforces vanishing current density. We can write the energy current in terms of the particle current by eliminating the electrochemical force, *viz.*,

$$\mathbf{j}_E = -\frac{L_{21}}{L_{11}}\mathbf{j}_p + \left(L_{22} - \frac{L_{12}L_{21}}{L_{11}}\right)\nabla\left(\frac{1}{T}\right). \tag{9}$$

Now, if we have an open circuit that prohibits particle currents ($\mathbf{j}_p = \mathbf{0}$), the thermal conductivity becomes

$$\kappa_{\text{open}} = \frac{1}{T^2}\left(L_{22} - \frac{L_{12}L_{21}}{L_{11}}\right). \tag{10}$$

Note that this choice implies that the flux associated with the temperature gradient ∇T is in instantaneous balance with the total electrochemical force. Which thermal conductivity is appropriate is, of course, problem dependent.

The SMT model used in subsequent sections is formulated based on the Chapman-Enskog expansion, which is detailed in Chapman and Cowling.[5] In subsection II A, we treat electrical conductivity, which, if assumed to be isothermal, is given by $\sigma = e^2 L_{11}/T$ when currents are driven by the *total* electrochemical force $\nabla\tilde{\mu}$. The electrical conductivity in CC is defined not in terms of the electrochemical potential but solely in terms of the electric field—see their Equation (19.13, 2). Then, in subsection II B, we turn to thermal conduction. To connect the convention of Onsager[14] with that of Chapman and Cowling (CC), it can be readily seen that Eqs. (6) and (7) of this document are analogous to Eqs. (8.4, 1) and (8.4, 3) in CC, respectively. By eliminating the diffusive flux (what CC call $\mathbf{d}_{12}$), CC then obtained Eq. (8.41,3), which is analogous to our Eq. (9); therefore, their expression (8.41, 4) is equivalent to the "open circuit" expression in Eq. (10).

Finally, in subsection II C, we discuss thermal diffusivity, which is defined by the relation (8.4, 7) from CC.

A. Electrical conductivity

We first turn to electrical conduction, which is the response of the particle flux to the presence of an electric field. As such, its calculation within the framework of the Boltzmann equation is similar to that of the inter-diffusion coefficient. For a system with only electrons and a single ionic species, it can be shown that the electrical conductivity will be proportionate to the inter-diffusion coefficient between these two charged species through the relation

$$\sigma = \frac{n_e n_i n (m_i + m_e Z_i)^2 e^2}{(m_e n_e + m_i n_i)^2 T} D_{ei} \approx \frac{n_e n e^2}{n_i T} D_{ei}, \tag{11}$$

where $n = n_e + n_i$ is the total number density.[5] The approximation here is obtained by exploiting the mass disparity between electrons and ions. The inter-diffusion coefficient can then be calculated as

$$D_{ei} = \frac{3T^{5/2}}{16\sqrt{2\pi\mu_{ei}} n Z^2 e^4 K_{11}(g_{ei})}, \tag{12}$$

where $\mu_{ei} = m_e m_i/(m_e + m_i) \approx m_e$ is the reduced mass. Note that electrons are assumed to have a positive charge in the calculation of $g_{ei} = Ze^2/(\lambda_{\text{eff}} T)$, making them effectively positrons.

For comparison, we draw upon the recently published results of the *Charged-Particle Transport Coefficient Code Comparison Workshop*, in which a multitude of contributors submitted transport coefficient calculations using a variety of methods.[17] For brevity, we have plotted the predictions of the SMT model against a subset of the results from,[17] as shown in Fig. 1. In particular, electrical conductivities for a hydrogen plasma at the mass densities of $\rho = \{0.1, 1, 10\}$ g/cm^3 are examined for a range of temperatures. The methods compared to include Kohn–Sham density functional theory molecular dynamics (KS-MD),[18,19] orbital-free density functional theory molecular dynamics (OF-MD),[20,21] pseudo-ion in jellium (PIJ),[22] pseudoatom molecular dynamics (PAMD),[23] average atom (AA) models,[24,25] and the Lee-More (LM) formulas based on kinetic theory.[26] In each plot, the vertical blue line in the plots indicates the temperature at which $T = E_F$. While the model incorporates degeneracy into the screening effects, it still uses a Maxwell–Boltzmann velocity distribution, so the prediction does not have the usual plateau when $T < E_F$. Although it is reasonable to expect this plateau in the degenerate regime, where the value would roughly be given by the intersection of the blue and black curves, more numerical work is needed to verify this conjecture. Additionally, the SMT model appears to predict systematically lower values of the electrical conductivity across all temperatures, which is not the case for the thermal conductivity.

There could be a variety of explanations for the lower values of the SMT model, and we have proposed several. First, the electrical conductivity relies on electron-ion interactions as opposed to the thermal conductivity, which relies on electron–electron interactions as well. As the SMT model assumes repulsive interactions, the electrons are in fact taken as positrons as mentioned previously. While the leading order value of transport coefficients are agnostic to the sign of the charges, a second-order error is still incurred (i.e., the Barkas effect). This said, these same errors are not observed in other transport coefficients that rely on electron-ion interactions (see Secs. III and IV), so the source of the error could be elsewhere. A more likely reason is that the electrical conductivity probes a lower velocity spectrum than thermal conductivity does; this is due to the fact that the former is

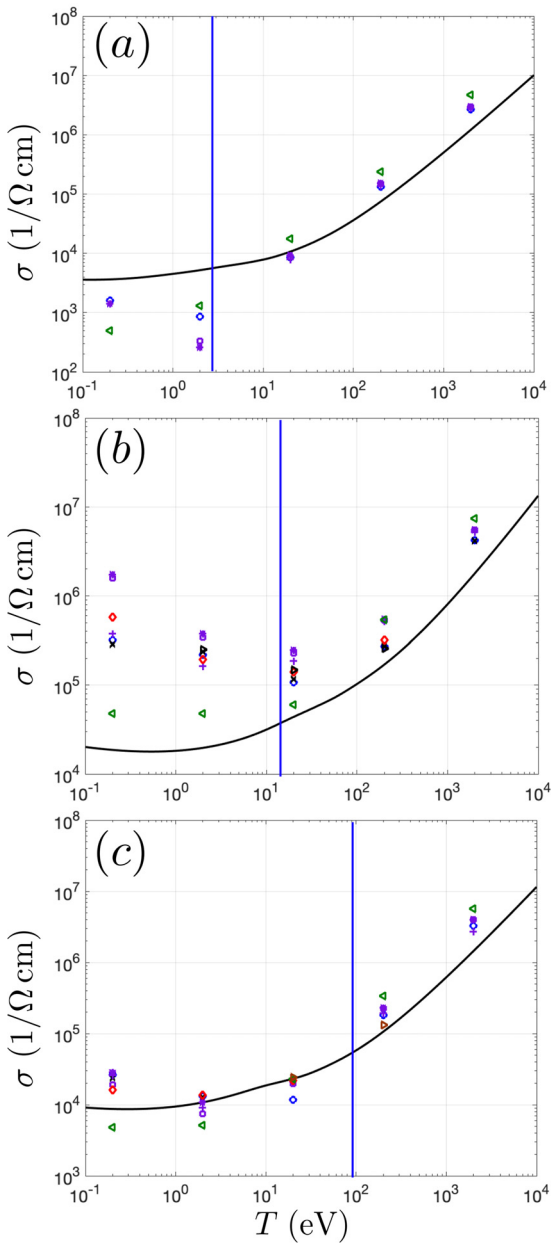

FIG. 1. Electrical conductivity predictions for H over a range of temperatures from various computational models: SMT (black, solid curve), PIJ (blue circles), OF-MD (black x-marks), KS-MD (red diamonds), LM (green triangles), PAMD (brown triangles), and AA (purple pluses, stars and squares). The comparisons are shown for the three mass densities (a) $\rho = 0.1$, (b) $\rho = 1$, and (c) $\rho = 10$ g/cm^3. In each subplot, the vertical blue line indicates the temperature at which the degeneracy is unity (i.e., $T = E_F$), where $T = \{2.8, 16, 85\}$ eV for subplots (a)–(c), respectively.

associated with mass flux and thus depends on the first-order velocity moment of the phase space distribution, $\langle v \rangle$, while the latter is associated with energy flux and thus depends on the third-order velocity moment, $\langle v^3 \rangle$. As such, the missing quantum mechanical effects associated with a lower distance of classical approach will be more relevant for electrical conductivity, thus giving rise to a breakdown of the SMT model.

We have also plotted the SMT prediction of electrical conductivity for the mixture case in Fig. 2, where the systematically lower values are observed again. While the generalization to mixtures for thermal conductivity is trivially captured through the effective screening length in Eq. (2), the explicit electron-ion interactions of electrical conductivity require a modification of the overall formula as well. To generalize Eq. (11) for a system with electrons and N ionic species, the interdiffusion coefficient D_{ei} must be calculated between the electrons and each ionic species, resulting in the relation

$$\sigma = \frac{n_e e^2}{T}\left(\sum_{i=1}^{N}\frac{x_i}{D_{ei}}\right)^{-1}, \tag{13}$$

where x_i is the number fraction out of the *total* number density $n = n_e + \sum_i n_i$, and we have again exploited the electron-ion mass disparity.[5] Equation (11) will clearly be recovered for the single ionic component case of $N = 1$. It can also be seen that the contribution of each ionic species combines additively to the electrical *resistance*, the inverse of the conductivity.

B. Thermal conductivity

Ionic thermal conductivity was discussed in Ref. 2, which we extend here to electronic thermal conductivity. When taking the electrons into account, the plasma must be viewed as a mixture, and the *total* thermal conductivity of the electron-ion system can be approximated as

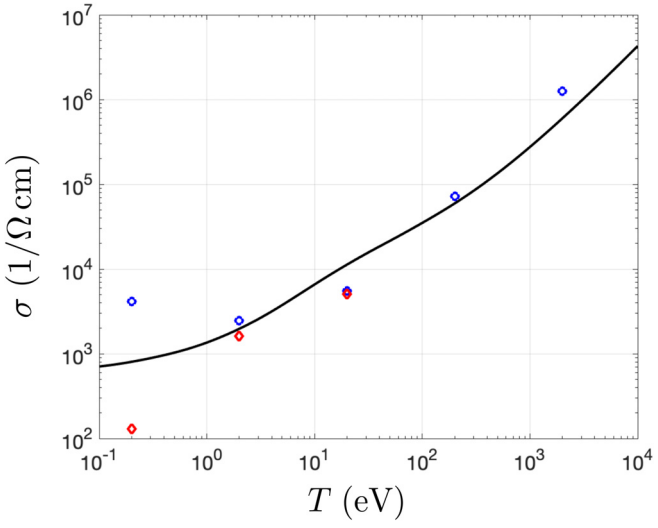

FIG. 2. Electrical conductivity predictions for a 50–50 CH mixture over a range of temperatures at a total mass density of $\rho = 1$ g/cm^3. The SMT model (black, solid curve) is compared to PIJ (blue circles) and KS-MD (red diamonds).

$$\kappa = \frac{x_i^2\mathcal{Q}_{ii}\kappa_{ii} + x_i x_e \mathcal{Q}'_{ei} + x_e^2\mathcal{Q}_{ee}\kappa_{ee}}{x_i^2\mathcal{Q}_{ii} + x_i x_e \mathcal{Q}_{ei} + x_e^2\mathcal{Q}_{ee}}, \tag{14}$$

where $x_j = n_j/(n_e + n_i)$ are the number density fractions, and the coefficients $\mathcal{Q}_{ij}$ are defined in Appendix A. Since $n_e = Zn_i$, these density fractions can also be expressed in terms of the mean ionization as $x_e = Z/(1+Z)$ and $x_i = 1/(1+Z)$. Finally, the self-conductivities are given as

$$\kappa_{jj} = \frac{75T^{5/2}}{64\sqrt{\pi m_j}(Z_j e)^4 \mathcal{K}_{22}(g_{jj})}, \tag{15}$$

with m_j being the electron or ion mass, and $g_{jj} = (Z_j e)^2/(\lambda_{\text{eff}} T)$. The function $\mathcal{K}_{22}(g_{jj})$ is the dimensionless collision integral, where the fits from[2] have been included again in Appendix B. The reduced conductivity can also be expressed in dimensionless form as

$$\kappa^* = \frac{25\sqrt{3\pi}}{48\Gamma^{5/2}\mathcal{K}_{22}(g_{ee})}, \tag{16}$$

where $\kappa^* = \kappa/(n_e\omega_p a_e^2)$. Here, $\omega_p = (4\pi n_e e^2/m_e)^{1/2}$ is the plasma frequency, and $a_e = (3/4\pi n_e)^{1/3}$ denotes the electron sphere radius. [Note that in Ref. 2, an error was made in writing $\kappa^* = \kappa/(m\omega_p a^2)$ instead of $\kappa^* = \kappa/(n\omega_p a^2)$.]

Exploiting the disparate mass ratio between the electrons and ions, the thermal conductivity can be approximated as

$$\kappa \approx \frac{Z\mathcal{Q}'_{ei}}{\mathcal{Q}_{ii} + Z\mathcal{Q}_{ei}} \approx \frac{75T^{5/2}}{16\sqrt{2\pi m_e}e^4\Lambda}, \tag{17}$$

where Λ can be thought of as a Coulomb logarithm-type of quantity and can be expressed as

$$\Lambda = Z[25\mathcal{K}_{11}(g_{ei}) - 20\mathcal{K}_{12}(g_{ei}) + 4\mathcal{K}_{13}(g_{ei})] + \sqrt{8}\mathcal{K}_{22}(g_{ee}). \tag{18}$$

Note that the quantity $[25\mathcal{K}_{11}(g) - 20\mathcal{K}_{12}(g) + 4\mathcal{K}_{13}(g)]$ is monotonically decreasing as a function of g and asymptotically approaches zero without going negative, so there is no possibility of (17) unphysically diverging in the strongly coupled regime.

We can again compare SMT to the same systems explored in Sec. II A as shown in Fig. 3. For these systems, the SMT model appears to agree well with other models beyond 10 eV, though the results are worse for higher densities. It should also be noted that at lower temperatures, the variation in model predictions can range by orders of magnitude although the actual conductivity values are so low that they are unlikely to affect hydrodynamic simulations.

Thermal conductivity values are also calculated for a 50–50 CH mixture with a total mass density of $\rho = 1$ g/cm^3 although there are far fewer simulations to compare to from the dataset in Ref. 17 Results are shown in Fig. 4 compared to both PIJ and KS-MD calculations with fairly good agreement. The dearth of results available for comparison highlights one of the primary advantages of the SMT model, which is its trivial implementation. Being only a function call, the SMT fits can be applied to an arbitrary number of species with little to no effect on the computational cost.

A further comparison can be made through the use of the Lorenz number, defined as $\mathcal{L} \equiv \kappa/\sigma T$.[27–29] For a single ionic species, the Lorenz number can then be approximated as

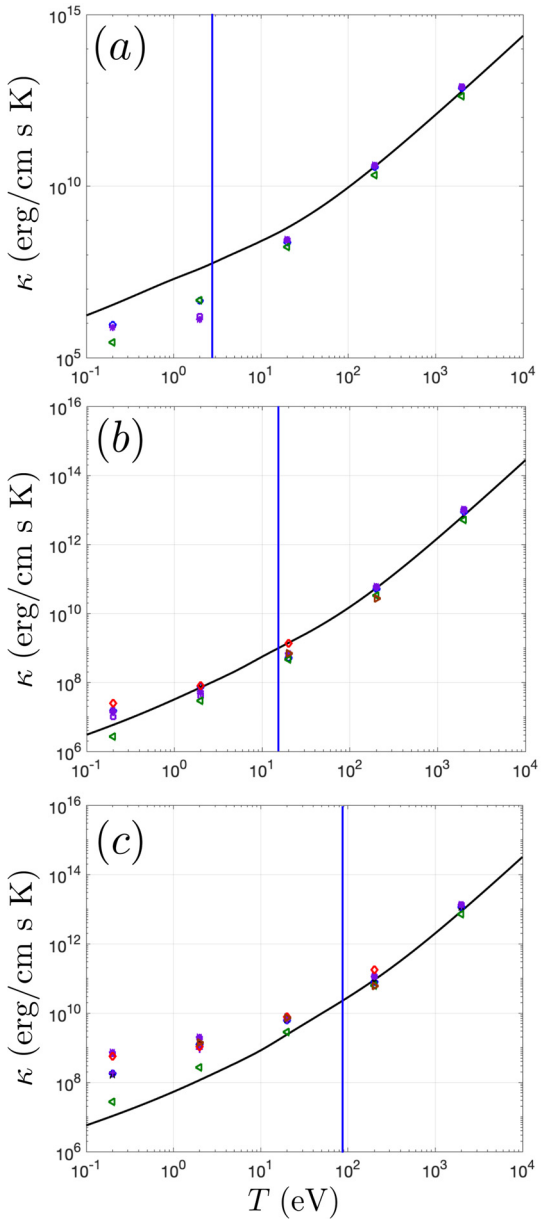

FIG. 3. Thermal conductivity predictions for H over a range of temperatures from various computational models: SMT (black, solid curve), PIJ (blue circles), OF-MD (black x-marks), KS-MD (red diamonds), LM (green triangles), PAMD (brown triangles), and AA (purple pluses, stars and squares). The comparisons are shown for the three mass densities (a) $\rho = 0.1$, (b) $\rho = 1$, and (c) $\rho = 10$ g/cm^3. In each subplot, the vertical blue line indicates the temperature at which the degeneracy is unity (i.e., $T = E_F$), where $T = \{2.8, 16, 85\}$ eV for subplots (a)–(c), respectively.

$$\mathcal{L} = \frac{25Z}{e^2\Lambda} K_{11}(g_{ei}), \tag{19}$$

where Λ is given in Eq. (18). Comparisons to this expression are shown in Fig. 5 as a function of temperature. We have additionally

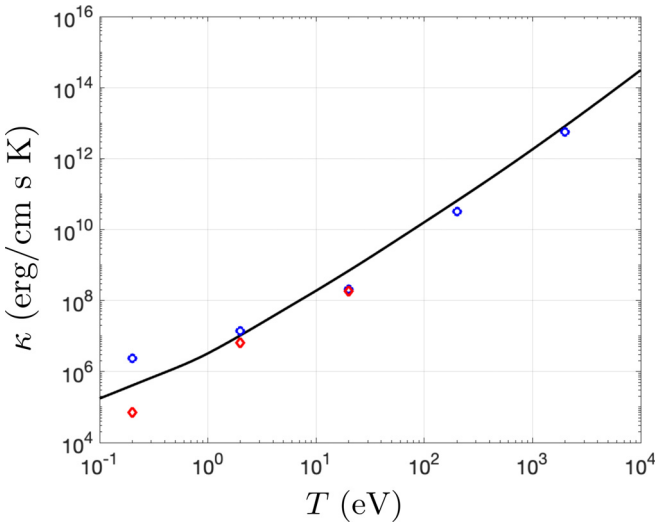

FIG. 4. Thermal conductivity predictions for a 50–50 CH mixture over a range of temperatures at a total mass density of $\rho = 1$ g/cm^3. The SMT model (black, solid curve) is compared to PIJ (blue circles) and KS-MD (red diamonds).

included an analytic expression proposed by Faussurier *et al.*,[28] which can be seen to agree well with the other simulations. Interestingly, the SMT model shows the strongest agreement in the degenerate limit, where the Lorenz number approaches the Wiedemann-Franz law, given by $\mathcal{L} = \pi^2 k_B^2/3e^2 \approx 2.44 \times 10^{-8}$ W Ω K^{-2}.[30] While there is a bit of scatter among all of the models, the SMT model is mostly consistent with the other models. While disagreement might be expected at lower temperatures, the opposite is in fact true; we speculate that this

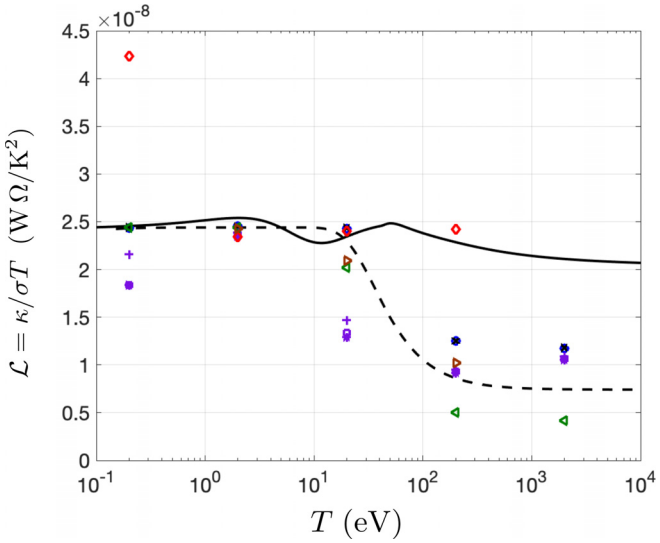

FIG. 5. Lorenz numbers for the case of H at $\rho = 10$ g/cm^3 from various computational models: SMT (black, solid curve), PIJ (blue circles), OF-MD (black x-marks), KS-MD (red diamonds), LM (green triangles), PAMD (brown triangles), and AA (purple pluses, stars and squares). An analytic formula from Faussurier *et al.* (black, dashed line) is given as well.

occurs because quantum mechanical scattering is more important at *high* temperatures. This suggests a very straightforward correction to the SMT model for hot plasmas that we intend to add in the future.

C. Other conductivity coefficients

While electrical and thermal conductivity are often the focus of particle and energy transport, Eqs. (6) and (7) contain contributions to particle and energy flow beyond those associated with these transport processes. For example, thermal diffusion is particle flow due to the presence of temperature gradients, which can be quantified by the L_{12} Onsager coefficient in Eq. (6) or the thermal diffusion ratio $k_T \equiv D_T/D_{ei}$ found in Equation (8.4, 7) of CC, where D_T is the thermal diffusion coefficient and D_{ei} is given in Eq. (12). Using again the disparity of the electron-ion mass ratio, an approximate form for k_T is given by

$$k_T \approx \frac{5Z^2}{(Z+1)\Lambda}[2K_{12}(g_{ei}) - 5K_{11}(g_{ei})], \tag{20}$$

where Λ is given in Eq. (18). The thermal diffusion ratio can be expressed in terms of the thermal diffusion factor as $k_T = x_i x_e \alpha_{ei}$. Note that, unlike most other transport coefficients, the thermal diffusion ratio and factor are not symmetric with respect to the species, as $\alpha_{ei} = -\alpha_{ie}$.

III. TEMPERATURE RELAXATION

Plasma experiments are typically multi-temperature as any plasma-formation process (e.g., radiation or shocks) will create electrons at a different temperature than the ions. Additionally, any mass disparities between various ion species can lead to distinct ionic temperature fields as well.[31] For this reason, it is important to have accurate models for the relevant temperature relaxation times τ_{ij} between two species (or equivalently the relaxation rates $\nu_{ij} = 1/\tau_{ij}$). This relaxation timescale can be calculated through the usual collision integrals as

$$\tau_{ij} = \frac{3(m_i + m_j)T_{ij}^{3/2}}{32\sqrt{2\pi\mu_{ij}}n_j Z_i^2 Z_j^2 e^4 \mathcal{K}_{11}(g_{ij})}, \tag{21}$$

where $\mu_{ij} = m_i m_j/(m_i + m_j)$ is again the reduced mass, and we have now introduced the notion of an inter-species temperature T_{ij}. Multiple models for T_{ij} have been proposed, but for the present work, we have chosen

$$T_{ij} = \frac{m_i T_j + m_j T_i}{m_i + m_j}, \tag{22}$$

which has been shown to be quite successful in modeling two-temperature systems.[32] In the case of electron-ion temperature relaxation, the mass ratio can be again exploited to obtain the simpler result of

$$\tau_{ei} \approx \frac{3m_i T_e^{3/2}}{32\sqrt{2\pi m_e}n_i Z_i^2 e^4 \mathcal{K}_{11}(g_{ei})}. \tag{23}$$

To show the general behavior of this form, we have plotted τ_{ei} as a function of T_e for various ionic number densities at $Z = 1$ in Fig. 6. The ionic temperature was set to $T_i = 100$ eV, which was largely an arbitrary choice, as the electron-ion relaxation time has little dependence on T_i for most relevant conditions. The ionic densities chosen were in the range $[10^{20}, 10^{26}]$, which is relevant to inertial confinement fusion conditions.

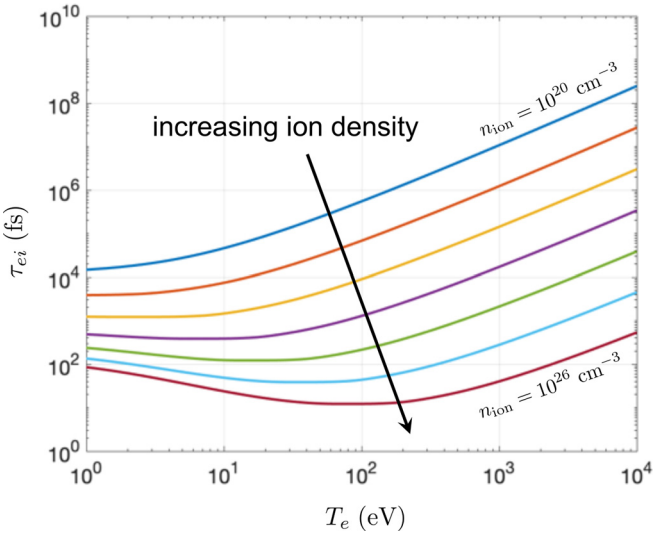

FIG. 6. Electron-ion temperature relaxation times as a function of T_e for various ionic number densities at $Z = 1$. The ionic temperature was set to $T_i = 100$ eV although there is little change to the curves when other values of T_i are used. The ionic densities were in the range $(10^{20}, 10^{26})$, which is relevant to inertial confinement fusion conditions.

For comparison of these results to a higher fidelity model, we turn to molecular dynamics (MD) simulations of Glosli *et al.*,[33] where temperature relaxation times of a hydrogen plasma are calculated using quantum statistical potentials.[34] The reported MD values (denoted by τ_{MD}) along with the prediction from the SMT model (denoted by τ_{SM}) are shown in Fig. 1. More specifically, the quantity $\tau_{MD} = 2/(\tau_{ei}^{-1} + \tau_{ie}^{-1})$ from the MD simulations is presented to account for the asymmetry of the rates (this corresponds to twice the value of τ^* shown in Table I of Ref. 33). Cases M_2 and M_3 were performed at the same conditions as in case M_1; however, they are distinguished by using quantum statistical potentials (M_2) and bare Coulomb potentials (M_3) for a positron-proton system to demonstrate the minimal effect of replacing electrons with positrons. From the values shown in Fig. 1, it can be seen that the SMT prediction was within 30% (though consistently lower than) of most of the MD results.

The largest deviations are associated with the $n_i = 10^{24}$ cm^{-3} cases; however, these cases are less comparable due to the presence of degenerate electrons (particularly in cases *F* and *G*). The SMT model incorporates degeneracy through the screened electrons, which has the effect of decreasing the relaxation times. For a better comparison with these MD simulations, which do not account for degeneracy, the SMT model was evaluated with a classical treatment of the electrons. The resulting relaxation times were $\tau_{SM} = 1.27 \times 10^2$ fs and $\tau_{SM} = 1.25 \times 10^2$ fs for cases *F* and *G*, respectively, which are within 30% of the MD results.

IV. STOPPING POWER

The final transport process we consider is stopping power, defined as the energy loss per unit length of charged particles due to

TABLE I. Comparison of temperature relaxation times between MD simulations from Ref. 33 and the SMT model for a variety of system parameters. The largest deviations observed are for cases in which the electron degeneracy is appreciable, and these deviations can be mitigated by neglecting degeneracy effects in the SMT model.

Case	n_i (cm^{-3})	T_e (eV)	T_i (eV)	τ_{MD} (fs)	τ_{SM} (fs)
A	10^{20}	10.0	20.0	4.08×10^4	4.03×10^4
B	10^{20}	30.0	60.0	1.58×10^5	1.28×10^5
C	10^{22}	10.0	20.0	1.05×10^3	1.37×10^3
D	10^{22}	30.0	60.0	3.46×10^3	2.74×10^3
E	10^{22}	100.0	200.0	1.29×10^4	8.82×10^3
F	10^{24}	10.0	20.0	1.77×10^2	7.54×10^1
G	10^{24}	30.0	60.0	1.65×10^2	1.09×10^2
H	10^{24}	100.0	200.0	3.44×10^2	2.10×10^2
I	10^{24}	300.0	600.0	8.34×10^2	5.56×10^2
J	1.6×10^{24}	29.9	80.1	4.04×10^2	7.88×10^1
K	1.6×10^{24}	91.47	12.1	2.40×10^2	1.38×10^2
L	10^{20}	100.0	200.0	7.30×10^5	5.39×10^5
M_1	10^{20}	10.0	40.0	4.10×10^4	4.03×10^4
M_2	10^{20}	10.0	40.0	4.36×10^4	4.03×10^4
M_3	10^{20}	10.0	40.0	4.56×10^4	4.03×10^4

scattering by a target material. Accurate stopping power models are of particular importance to understanding energy deposition in high energy-density plasmas undergoing fusion reactions.[35–37] Unlike other transport coefficients, stopping power depends on a projectile velocity (v_p) rather than an average over thermal velocities,

$$\mathcal{S}(v_p) = -\frac{dE}{dx}, \tag{24}$$

which means that the usual collision integrals cannot be used. One solution is to modify the effective screening length (2) to incorporate finite-velocity effects. The effective interactions between ions will become more Coulomb-like at higher velocities as the screening background is unable to respond quickly. Zwicknagel *et al.*[38] suggested the following form to modify the ionic screening length:

$$\lambda_i(v) = \left(1 + \left(\frac{v}{v_i}\right)^2\right)^{1/2} \lambda_i, \tag{25}$$

where we have introduced the thermal velocity of the ith species as $v_i = (2T/m_i)^{1/2}$ although this is not a unique choice. As shown by Grabowski *et al.*,[39] the modification (25) yields surprisingly good agreement. The resulting velocity-dependent effective screening length will then take the form

$$\lambda_{\mathrm{eff}}(v) = \left(\frac{1}{\lambda_e^2} + \sum_i \frac{1}{\lambda_i^2}\left(\frac{1}{1 + v^2/v_i^2 + 3\Gamma_i}\right)\right)^{-1/2}. \tag{26}$$

The underlying binary approximation of the Boltzmann equation framework allows the stopping power to be decomposed into the interactions of a given projectile and each species within the target material,

$$\mathcal{S}(v_p) = \sum_k \mathcal{S}_k(v_p), \quad \mathcal{S}_k(v_p) = -\frac{dE_k}{dx}(v_p), \tag{27}$$

where the index k sums over all species in the target (including the electrons). We can thus express the stopping power from each contribution in terms of the projectile velocity as

$$\mathcal{S}_k(v_p) = \frac{m_k n_k v_k}{2\sqrt{\pi} v_p^2} \int_0^\infty dv\, v^2 \sigma_{kp}^{(1)}(v)(F_+^k - F_-^k), \tag{28}$$

$$F_\pm^k(v; v_p) = \left(1 \pm 2\frac{v_p v}{v_k^2}\right) e^{-\left(\frac{v \pm v_p}{v_k}\right)^2}. \tag{29}$$

The momentum transfer cross section will now have additional velocity dependencies through the effective screening length,

$$\sigma_{kp}^{(1)}(v) = 2\pi\lambda_{\mathrm{eff}}^2(v)\phi_1(w), \quad w^2 = \frac{\mu\lambda_{\mathrm{eff}}(v)}{2Z_k Z_p e^2} v^2, \tag{30}$$

where fits to $\phi_n(w)$ can be found in Appendix B. To examine the validity of the SMT model, we consider the stopping of an alpha particle in a hydrogen plasma with an ionic number density of $n_{\mathrm{ion}} = 1.03 \times 10^{20}\ \mathrm{cm}^{-3}$ and a temperature of 10.9 eV. For comparison, we employ both the model of Brown, Preston and Singleton (BPS)[40,41] and MD simulations performed by Surh *et al.* using quantum statistical potentials.[42] The results of this comparison are shown in Fig. 7 with the SMT model showing good agreement with both BPS and MD. This particular system is weakly coupled ($\Gamma \sim 0.1$); however, the SMT model is not restricted to this regime as many other stopping power models are. While the SMT model will eventually lose its accuracy for sufficiently large coupling, it has the desired feature of staying bounded across the entire parameter space.

A key quantity of interest that can be extracted from a stopping power model is the relative amount of energy deposited into each target species by the projectile. Given the ease of calculating stopping

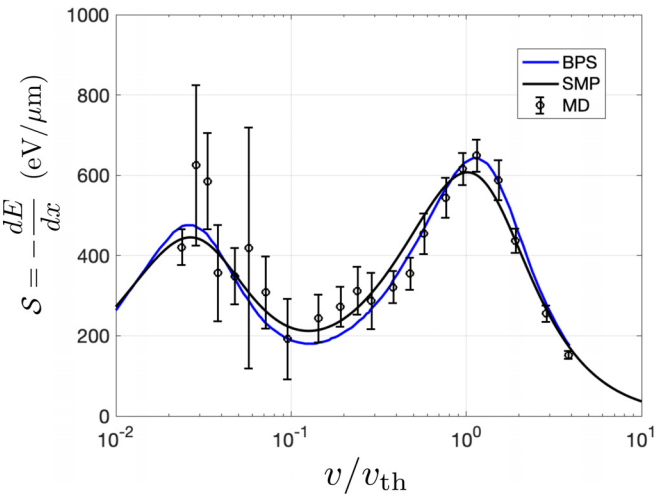

FIG. 7. Stopping power calculations using the SMT model (black curve), BPS model (blue curve) and MD (black points) for an alpha particle stopping in a hydrogen plasma at $n_i = 1.03 \times 10^{20}\ \mathrm{cm}^{-3}$ and $T = 10.9$ eV. Results are expressed as a function of the projectile velocity reduced by the ion thermal velocity.

power curves with the SMT model, determining this energy split is fairly straightforward and obtained by integrating the equations of motion for the projectile,

$$\frac{dv_p}{dt} = \frac{1}{m_p}\sum_k \frac{dE_k}{dx}, \tag{31}$$

while tracking the energy deposition into each species along the entire trajectory. As an example, we consider an alpha particle with an initial energy of 3.5 MeV in a hydrogen plasma having an ionic number density of $n_{\text{ion}} = 10^{24}$ cm^{-3} and a range temperatures. The results of these simulations are shown as the percentage of energy deposited into the ions (hydrogen) for $0 < T < 40$ keV in Fig. 8, where we have also included a dashed line indicating the value $T = 5$ eV, which is the current highest reported temperature for an ignition-path shot at the National Ignition Facility.[43]

A fit to these results yields the following approximate form for the fraction of energy deposited into the ions:

$$f_{\text{ion}}(T) \approx \frac{T}{T + T_0}, \tag{32}$$

where $T_0 = 16$ keV. The normalized $\mathcal{L}^2$-norm of the relative error between the fit and the data was 0.033 for this value of T_0, which is further discussed in Appendix C. Interestingly, the functional form of the fit is identical to the one determined by Fraley *et al.*;[44] however, their calculations resulted in the value $T_0 = 32$ keV. The numerical values used to determine (32) are presented in Appendix C for the convenience of the reader.

V. CONCLUSION

It is desirable to have a single, rapid, self-consistent model that treats a wide range of plasma mixture properties, including both electronic and ionic, over wide ranges of temperature and density. Toward this goal, we examined the use of the SMT model,[2] which was originally intended to describe transport processes associated with classical, repulsive interactions, to a variety of electronic transport properties. In particular, the utility of the SMT model for thermal conductivity, electrical conductivity, temperature relaxation, and stopping power was explored.

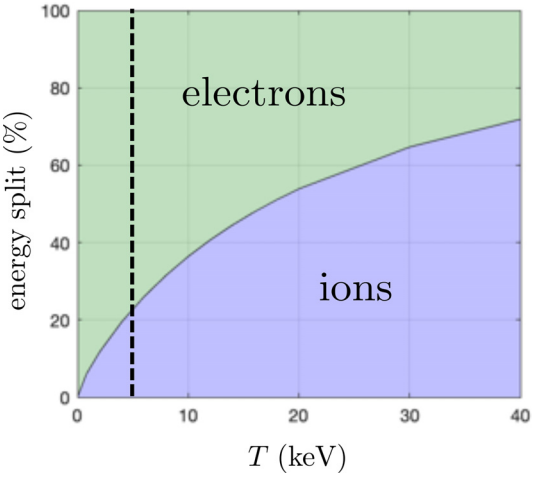

FIG. 8. Energy split due to alpha stopping with an initial energy of 3.5 MeV in a hydrogen plasma at $n_i = 10^{24}$ cm^{-3}. The percentage of energy deposited by the projectile into the ions is shown as a function of target temperature. The vertical dashed line corresponds to $T = 5$ eV, which is the current highest reported temperature for an ignition-path shot at the National Ignition Facility.[43]

For thermal and electrical conductivity, we use the recently published results from the *Charged-Particle Transport Coefficient Code Comparison Workshop*,[17] which includes simulations from higher fidelity physics models for a variety of transport coefficients across the parameter space. Large agreement was observed between SMT and the available data for thermal conductivity although systematic deviations are observed for electrical conductivity. It is suspected that the lower velocity spectrum probed by electrical conductivity necessitates a more quantum mechanical treatment of the scattering physics.

With regard to temperature relaxation, MD simulation data from Ref. 33 are used for validation, where most results were within 30% of the SMT prediction. Due to the multi-temperature nature of these systems, the SMT model was generalized to allow for cross-temperatures. The largest deviations occurred for dense systems with degenerate electrons, and as these particular MD simulations did not account for degeneracy, the deviations were lessened by neglecting degenerate electron screening in the SMT model.

Finally, stopping power was considered, which precluded the use of the standard collision integrals in SMT as the cross sections are necessarily velocity-resolved for this process. Instead, a velocity-dependent screening length was used to construct a more accurate cross section, and the resulting calculations were compared to both MD and the BPS model with good agreement. Furthermore, the stopping power calculations enabled the determination of relative energy deposition into each target species from the projectile as a function of system temperature, where a simple yet accurate fit to the energy split was provided.

Despite its simplicity and semi-classical foundations, the SMT model offers an extremely efficient opinion of electronic transport coefficients that is fairly accurate across a large range of the parameter space. Furthermore, there is little to no computational cost associated with adding multiple ionic components, which makes the SMT model ideal for many dense plasma applications. Based on the reasonable accuracy of our results for several electronic transport coefficients, we propose to use the SMT model to self-consistently compute all transport coefficients. To do this, an equation of state for mixtures is needed to produce the plasma mixtures ionization states and free electron density.[31,45,46] From the mixture properties, the basic inputs into the SMT framework can be obtained and then used to evaluate the fits for each of the independent electronic and ionic coefficients. Future work would entail a more quantum mechanical treatment of both the cross sections and the collision integrals as well as generalizing the SMT model to attractive interactions.

ACKNOWLEDGMENTS

This research was supported in part by U.S. Air Force Office of Scientific Research Grant No. FA9550-17-1-0394. The authors would especially like to thank Michael P. Surh, James N. Glosli, David F. Richards, and Frank R. Graziani at Lawrence Livermore National Laboratory for providing stopping power simulation data.

APPENDIX A: THERMAL CONDUCTIVITY COEFFICIENTS

Here, we present the coefficients associated with calculating the thermal conductivity. For consistency, we use notation similar to that of CC,[5]

$$\mathcal{Q}_{ii} = \mathcal{P}_i(6M_e^2 + (5-4\mathcal{B})M_i^2 + 8M_eM_i\mathcal{A}), \tag{A1}$$

$$\mathcal{Q}_{ee} = \mathcal{P}_e(6M_i^2 + (5-4\mathcal{B})M_e^2 + 8M_eM_i\mathcal{A}), \tag{A2}$$

$$\mathcal{Q}_{ei} = 3(M_i - M_e)^2(5-4\mathcal{B}) + 2\mathcal{P}_e\mathcal{P}_i + 4M_eM_i\mathcal{A}(11-4\mathcal{B}), \tag{A3}$$

$$\mathcal{Q}'_{ei} = \frac{15T(\mathcal{P}_e + \mathcal{P}_i + (11-4\mathcal{B}-8\mathcal{A})M_eM_i)}{16(m_e+m_i)M_eM_i\Omega_{ei}^{(1,1)}}, \tag{A4}$$

$$\mathcal{A} = \frac{\Omega_{ei}^{(2,2)}}{5\Omega_{ei}^{(1,1)}}, \quad \mathcal{B} = \frac{5\Omega_{ei}^{(1,2)} - \Omega_{ei}^{(1,3)}}{5\Omega_{ei}^{(1,1)}}, \tag{A5}$$

$$\mathcal{P}_i = \frac{\Omega_{ii}^{(2,2)}}{5M_e\Omega_{ei}^{(1,1)}}, \quad \mathcal{P}_e = \frac{\Omega_{ee}^{(2,2)}}{5M_i\Omega_{ei}^{(1,1)}}, \tag{A6}$$

$$M_i = \frac{m_i}{m_i+m_e}, \; M_e = \frac{m_e}{m_i+m_e}. \tag{A7}$$

Fits to the collision integrals are presented in Ref. 2 and have been repeated again in Appendix B for completeness. The disparate electron-ion mass ratio allows $\mu = m_e/m_i$ to be an expansion parameter (not to be confused with the reduced mass μ_{ij}). The leading order coefficients then become

$$\mathcal{Q}_{ii} \approx \mathcal{P}_i(5-4\mathcal{B}) = \mathcal{O}(\mu^{-1}), \tag{A8}$$

$$\mathcal{Q}_{ee} \approx 6\mathcal{P}_e = \mathcal{O}(1), \tag{A9}$$

$$\mathcal{Q}_{ei} \approx 2\mathcal{P}_e\mathcal{P}_i = \mathcal{O}(\mu^{-1}), \tag{A10}$$

$$\mathcal{Q}'_{ei} \approx \frac{15T\mathcal{P}_i}{16m_i\mu\Omega_{ei}^{(1,1)}} \approx \frac{15T^{5/2}\mathcal{P}_i}{16\sqrt{2\pi m_e}Z^2e^4\mathcal{K}_{11}(g_{ei})}. \tag{A11}$$

APPENDIX B: NUMERICAL EVALUATION OF INTEGRALS

Momentum-transfer cross sections and collision integrals are numerically calculated and fitted in Ref. 2, and to make this document self-contained, we have included these same fits here as well. Each fit is piece-wise and was constructed to maintain $\mathcal{C}^1$-continuity, recover the appropriate asymptotic limits, and minimize the relative error between the fits and the numerical calculations.

The momentum-transfer cross section can be expressed in terms of a dimensionless cross section and velocity as

$$\sigma_{ij}^{(n)}(w,\lambda) = 2\pi\lambda^2\phi_n(w), \quad w^2 = \frac{\mu\lambda}{2Z_iZ_je^2}v^2. \tag{B1}$$

Here, the screening length λ can be taken as (2) or any other screening length that might be more appropriate. The function $\phi_n(w)$ can be decomposed into weak- and strong-coupling regimes as

$$\phi_n(w) = \begin{cases} \phi_n^{\mathrm{sc}}(w), & w < 1 \\ \phi_n^{\mathrm{wc}}(w), & w > 1, \end{cases} \tag{B2}$$

where the "strongly coupled" component is approximated by

$$\phi_n^{\mathrm{sc}}(w) \approx \frac{c_0 + c_1\ln(w) + c_2\ln^2(y) + c_3\ln^3(w)}{1 + c_4\ln(w)}, \tag{B3}$$

and the "weakly coupled" component is approximated by

$$\phi_n^{\mathrm{wc}}(w) \approx \frac{n}{2w^4}\ln(1+w^2)P(w), \tag{B4}$$

$$P(w) = \left[\frac{d_0 + d_1\ln(w) + d_2\ln^2(w) + \ln^3(w)}{d_3 + d_4\ln(w) + d_5\ln^2(w) + \ln^3(w)}\right]. \tag{B5}$$

The coefficients for (B3) and (B5) are presented for $n = \{1, 2\}$ in Table II although only the $n = 1$ is necessary for the stopping power calculations performed in this work.

Similarly, collision integrals can expressed in terms of dimensionless variables,

$$\Omega_{ij}^{(n,m)} = \sqrt{\frac{2\pi}{\mu_{ij}}}\frac{(Z_iZ_je^2)^2}{T^{3/2}}\mathcal{K}_{nm}(g), \quad g = \frac{Z_iZ_je^2}{\lambda T}. \tag{B6}$$

The function $\mathcal{K}_{nm}(g)$ can also be decomposed into weak- and strong-coupling regimes as

$$\mathcal{K}_{nm}(g) = \begin{cases} \mathcal{K}_{nm}^{\mathrm{wc}}(g), & g < 1 \\ \mathcal{K}_{nm}^{\mathrm{sc}}(g), & g > 1, \end{cases} \tag{B7}$$

where the weakly coupled component is approximated by

$$\mathcal{K}_{nm}^{\mathrm{wc}}(g) \approx -\frac{n}{4}(m-1)!\ln\left(\sum_{k=1}^{5}a_kg^k\right), \tag{B8}$$

and the strongly coupled component is approximated by

$$\mathcal{K}_{nm}^{\mathrm{sc}}(g) \approx \frac{b_0 + b_1\ln(g) + b_2\ln^2(g)}{1 + b_3g + b_4g^2}. \tag{B9}$$

The coefficient values are presented in Table III for the (n, m) pairs relevant to first-order Chapman–Enskog theory.

APPENDIX C: ENERGY SPLIT DATA AND FIT

The data for the energy split calculations are presented in Table IV. These data points were then fit to a functional form of the

TABLE II. Coefficients for fits (B3)–(B5) of the reduced cross sections (B1).

n	1	2
c_0	0.300 31	0.406 88
c_1	−0.691 61	−0.864 25
c_2	0.596 07	0.774 61
c_3	−0.398 22	−0.344 71
c_4	−0.206 85	−0.276 26
d_0	0.485 16	0.830 61
d_1	1.660 45	1.052 29
d_2	−0.886 87	−0.599 02
d_3	0.559 90	1.415 00
d_4	1.657 98	0.788 74
d_5	−1.024 57	−0.481 55

TABLE III. Coefficients for fits (B8)–(B9) of the reduced collision integrals (B6).

(n, m)	(1, 1)	(1, 2)	(1, 3)	(2, 2)
a_1	1.466 0	0.520 94	0.303 46	0.854 01
a_2	−1.783 6	0.251 53	0.237 39	−0.228 98
a_3	1.431 3	−1.133 7	−0.621 67	−0.600 59
a_4	−0.558 33	1.215 5	0.561 10	0.805 91
a_5	0.061 162	−0.437 84	−0.180 46	−0.305 55
b_0	0.081 033	0.205 72	0.683 75	0.434 75
b_1	−0.091 336	−0.165 36	−0.384 59	−0.211 47
b_2	0.051 760	0.061 572	0.107 11	0.111 16
b_3	−0.500 26	−0.127 70	0.106 49	0.196 65
b_4	0.170 44	0.066 993	0.028 760	0.151 95

TABLE IV. Numerical results of energy split calculations using the SMT model. The percentage (%) of energy deposited into the ions by an alpha particle in a hydrogen plasma is displayed for the given system temperature (keV).

T (keV)	Ions (%)
0	0.0000
0.8	5.9698
2	11.7214
4	19.4941
6	25.9565
8	31.5141
10	36.3780
12	40.6808
14	44.5172
16	47.9577
18	51.0641
20	53.8793
30	64.6779
40	71.8610

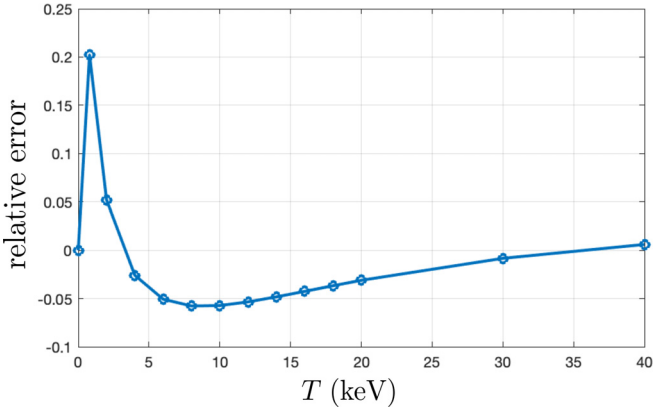

FIG. 9. Relative error between the data in Table IV and the approximate fit in Eq. (32). The highest errors can be seen near 1 keV.

ratio of two polynomials. While higher polynomials were explored, a surprising accuracy was found with the ratio of two linear polynomials in the form of Eq. (32). The resulting relative error between this fit and the data is shown in Fig. 9. However, the reader can use the data presented to construct a more accurate fit if necessary.

DATA AVAILABILITY

The data that support the findings of this study are available from the corresponding authors upon reasonable request.

REFERENCES

[1]Y. Ping, H. D. Whitley, A. McKelvey, G. E. Kemp, P. A. Sterne, R. Shepherd, M. Marinak, R. Hua, F. N. Beg, and J. H. Eggert, "Heat-release equation of state and thermal conductivity of warm dense carbon by proton differential heating," Phys. Rev. E **100**(4), 043204 (2019).
[2]L. G. Stanton and M. S. Murillo, "Ionic transport in high-energy-density matter," Phys. Rev. E **93**(4), 043203 (2016).
[3]H. A. Gould and H. E. DeWitt, "Convergent kinetic equation for a classical plasma," Phys. Rev. **155**(1), 68 (1967).
[4]R. H. Williams and H. E. DeWitt, "Quantum-mechanical plasma transport theory," Phys. Fluids **12**(11), 2326–2342 (1969).
[5]S. Chapman, T. G. Cowling, and D. Burnett, *The Mathematical Theory of Non-Uniform Gases: An account of the Kinetic Theory of Viscosity, Thermal Conduction and Diffusion in Gases* (Cambridge University Press, 1990).
[6]C. Paquette, C. Pelletier, G. Fontaine, and G. Michaud, "Diffusion coefficients for stellar plasmas," Astrophys. J., Suppl. Ser. **61**, 177–195 (1986).
[7]R. L. Liboff, "Transport coefficients determined using the shielded coulomb potential," Phys. Fluids **2**(1), 40–46 (1959).
[8]M. S. Murillo, J. Weisheit, S. B. Hansen, and M. W. C. Dharma-Wardana, "Partial ionization in dense plasmas: Comparisons among average-atom density functional models," Phys. Rev. E **87**(6), 063113 (2013).
[9]R. Phillips Feynman, N. Metropolis, and E. Teller, "Equations of state of elements based on the generalized Fermi–Thomas theory," Phys. Rev. **75**(10), 1561 (1949).
[10]R. M. More, "Pressure ionization, resonances, and the continuity of bound and free states," Adv. At. Mol. Phys. **21**, 305–356 (1985).
[11]F. M. Smith, W. Birnbaum, and W. H. Barkas, "Measurements of meson masses and related quantities," Phys. Rev. **91**(3), 765 (1953).
[12]W. H. Barkas, W. Birnbaum, and F. M. Smith, "Mass-ratio method applied to the measurement of l-meson masses and the energy balance in pion decay," Phys. Rev. **101**(2), 778 (1956).
[13]B. F. Rozsnyai, "Electron scattering in hot/warm plasmas," High Energy Density Phys. **4**(1–2), 64–72 (2008).
[14]H. B. Callen, "The application of Onsager's reciprocal relations to thermoelectric, thermomagnetic, and galvanomagnetic effects," Phys. Rev. **73**(11), 1349 (1948).
[15]A. Feldhoff, "Thermoelectric material tensor derived from the Onsager–de Groot–Callen model," Energy Harvesting Syst. **2**(1), 5–13 (2015).
[16]C. Goupil, W. Seifert, K. Zabrocki, E. Müller, and G. J. Snyder, "Thermodynamics of thermoelectric phenomena and applications," Entropy **13**(8), 1481–1517 (2011).
[17]P. E. Grabowski, S. B. Hansen, M. S. Murillo, L. G. Stanton, F. R. Graziani, A. B. Zylstra, S. D. Baalrud, P. Arnault, A. D. Baczewski, L. X. Benedict *et al.*, "Review of the first charged-particle transport coefficient comparison workshop," High Energy Density Phys. **37**, 100905 (2020).
[18]T. Sjostrom and J. Daligault, "Ionic and electronic transport properties in dense plasmas by orbital-free density functional theory," Phys. Rev. E **92**(6), 063304 (2015).
[19]M. P. Desjarlais, C. R. Scullard, L. X. Benedict, H. D. Whitley, and R. Redmer, "Density-functional calculations of transport properties in the nondegenerate limit and the role of electron-electron scattering," Phys. Rev. E **95**(3), 033203 (2017).
[20]F. Lambert, J. Clérouin, S. Mazevet, and D. Gilles, "Properties of hot dense plasmas by orbital-free molecular dynamics," Contrib. Plasma Phys. **47**(4–5), 272–280 (2007).

[21]F. Lambert, J. Clérouin, J.-F. Danel, L. Kazandjian, and S. Mazevet, "Properties of hot and dense matter by orbital-free molecular dynamics," in *Recent Progress in Orbital-Free Density Functional Theory* (World Scientific, 2013), pp. 165–201.
[22]P. Arnault, "Modeling viscosity and diffusion of plasma for pure elements and multicomponent mixtures from weakly to strongly coupled regimes," High Energy Density Phys. **9**(4), 711–721 (2013).
[23]C. E. Starrett, J. Daligault, and D. Saumon, "Pseudoatom molecular dynamics," Phys. Rev. E **91**(1), 013104 (2015).
[24]G. Gregori, S. B. Hansen, R. Clarke, R. Heathcote, M. H. Key, J. King, R. I. Klein, N. Izumi, A. J. Mackinnon, S. J. Moon *et al.*, "Experimental characterization of a strongly coupled solid density plasma generated in a short-pulse laser target interaction," Contrib. Plasma Phys. **45**(3–4), 284–292 (2005).
[25]S. B. Hansen, A. Y. Faenov, T. A. Pikuz, K. B. Fournier, R. Shepherd, H. Chen, K. Widmann, S. C. Wilks, Y. Ping, H. K. Chung *et al.*, "Temperature determination using k α spectra from M-shell Ti ions," Phys. Rev. E **72**(3), 036408 (2005).
[26]Y. T. Lee and R. M. More, "An electron conductivity model for dense plasmas," Phys. Fluids **27**(5), 1273–1286 (1984).
[27]C. Wang, X.-T. He, and P. Zhang, "*Ab initio* simulations of dense helium plasmas," Phys. Rev. Lett. **106**(14), 145002 (2011).
[28]G. Faussurier, C. Blancard, P. Combis, and L. Videau, "Electrical and thermal conductivities in dense plasmas," Phys. Plasmas **21**(9), 092706 (2014).
[29]H.-S. Kim, Z. M. Gibbs, Y. Tang, H. Wang, and G. J. Snyder, "Characterization of Lorenz number with Seebeck coefficient measurement," APL Mater. **3**(4), 041506 (2015).
[30]M. Z. John, *Principles of the Theory of Solids* (Cambridge University Press, 1972).
[31]L. G. Stanton, J. N. Glosli, and M. S. Murillo, "Multiscale molecular dynamics model for heterogeneous charged systems," Phys. Rev. X **8**(2), 021044 (2018).
[32]P. Seuferling, J. Vogel, and C. Toepffer, "Correlations in a two-temperature plasma," Phys. Rev. A **40**(1), 323 (1989).
[33]J. N. Glosli, F. R. Graziani, R. M. More, M. S. Murillo, F. H. Streitz, M. P. Surh, L. X. Benedict, S. Hau-Riege, A. B. Langdon, and R. A. London, "Molecular dynamics simulations of temperature equilibration in dense hydrogen," Phys. Rev. E **78**(2), 025401 (2008).
[34]J. P. Hansen and I. R. McDonald, "Thermal relaxation in a strongly coupled two-temperature plasma," Phys. Lett. A **97**(1–2), 42–44 (1983).
[35]M. Roth, T. E. Cowan, M. H. Key, S. P. Hatchett, C. Brown, W. Fountain, J. Johnson, D. M. Pennington, R. A. Snavely, S. C. Wilks *et al.*, "Fast ignition by intense laser-accelerated proton beams," Phys. Rev. Lett. **86**(3), 436 (2001).
[36]J. D. Lindl, P. Amendt, R. L. Berger, S. G. Glendinning, S. H. Glenzer, S. W. Haan, R. L. Kauffman, O. L. Landen, and L. J. Suter, "The physics basis for ignition using indirect-drive targets on the national ignition facility," Phys. Plasmas **11**(2), 339–491 (2004).
[37]D. A. Callahan-Miller and M. Tabak, "Progress in target physics and design for heavy ion fusion," Phys. Plasmas **7**(5), 2083–2091 (2000).
[38]G. Zwicknagel, "Nonlinear energy loss of heavy ions in plasma," Nucl. Instrum. Methods Phys. Res., Sect. B **197**(1–2), 22–38 (2002).
[39]P. E. Grabowski, M. P. Surh, D. F. Richards, F. R. Graziani, and M. S. Murillo, "Molecular dynamics simulations of classical stopping power," Phys. Rev. Lett. **111**(21), 215002 (2013).
[40]L. S. Brown, D. L. Preston, and R. L. Singleton, Jr., "Charged particle motion in a highly ionized plasma," Phys. Rep. **410**(4), 237–333 (2005).
[41]R. L. Singleton, "An exact calculation of electron-ion energy splitting in a hot plasma," Technical Report No. LA-UR-12-24620 (Los Alamos National Laboratory (LANL), Los Alamos, NM, 2012).
[42]M. P. Surh, J. N. Glosli, D. F. Richards, and F. R. Graziani, Personal communication (December 1, 2015).
[43]P. K. Patel, P. T. Springer, C. R. Weber, L. C. Jarrott, O. A. Hurricane, B. Bachmann, K. L. Baker, L. F. Berzak Hopkins, D. A. Callahan, D. T. Casey *et al.*, "Hotspot conditions achieved in inertial confinement fusion experiments on the National Ignition Facility," Phys. Plasmas **27**(5), 050901 (2020).
[44]G. S. Fraley, E. J. Linnebur, R. J. Mason, and R. L. Morse, "Thermonuclear burn characteristics of compressed deuterium-tritium microspheres," Phys. Fluids **17**(2), 474–489 (1974).
[45]J. Yuan, "Self-consistent average-atom scheme for electronic structure of hot and dense plasmas of mixture," Phys. Rev. E **66**(4), 047401 (2002).
[46]M. R. Zaghloul, M. A. Bourham, and J. Michael Doster, "A simple formulation and solution strategy of the Saha equation for ideal and nonideal plasmas," J. Phys. D: Appl. Phys. **33**(8), 977 (2000).